Journal of Alloys and Compounds 903 (2022) 163840

Contents lists available at ScienceDirect

Journal of Alloys and Compounds

journal homepage: www.elsevier.com/locate/jalcom

α−Ag_2WO_4 under microwave, electron beam and femtosecond laser irradiations: Unveiling the relationship between morphology and photoluminescence emissions

Mayara Mondego Teixeira[a,1,2,*], Lílian Cruz Santos[a,1,3], Ana Cristina Mora Tello[a,1,4,*], Priscila Barros Almeida[a,1,5], Jussara Soares da Silva[a,1,6], Letícia Laier[b,1,7], Lourdes Gracia[c,d,8], Marcio Daldin Teodoro[e,9], Luís Fernando da Silva[e,10], Juan Andrés[c,11], Elson Longo[a,12,*]

[a] Departamento de Química, CDMF, Universidade Federal de São Carlos, 13565-905 São Carlos, São Paulo, Brazil
[b] Laboratório Interdisciplinar em Cerâmica, Departamento de Físico-Química, Instituto de Química, UNESP, 14800-900 Araraquara, São Paulo, Brazil
[c] Departamento de Química Física i Analítica, University Jaume I, 12071 Castelló de la Plana, Spain
[d] Departamento de Química Física, Universitat de València, 46100 Burjassot, Spain
[e] Departamento de Física, Universidade Federal de São Carlos, 13565-905 São Carlos, São Paulo, Brazil

ARTICLE INFO

Article history:
Received 18 July 2021
Received in revised form 3 December 2021
Accepted 12 January 2022
Available online 19 January 2022

Keywords:
α−Ag_2WO_4
Electron beam irradiation
Femtosecond laser irradiation
Photoluminescence
Morphology
Surface band gap

ABSTRACT

In this study, the α-Ag_2WO_4 samples were successfully synthesized combined two methods, co-precipitation and microwave-assisted hydrothermal. Later, two different irradiation processes: electron beam and femtosecond laser are applied. Unit cell changes were shown by X-ray measurements and Rietveld analysis and compared with the results obtained for first-principle calculations. The formation of oxygen vacancies on the surface of the particles after the irradiation process was revealed by XPS measurements. Electron beam and femtosecond laser irradiations were found to cause expansion of the unit cell, form oxygen vacancies on the surface, change the angle and distance between O−Ag and O−W bonds, and modify the particle morphology to rod-, cube- and sphere-like. The XANES measurements confirm that the local order of the W atoms is maintained along the different irradiation processes. Based on the theoretical analysis of surfaces investigation and Wulff construction, the contribution of (010) and (101) surfaces at the emission centers in 550 and 733 nm associated with the PL spectrum of α–Ag_2WO_4, was established

1. Introduction

Recently, alpha-silver tungstate (α-Ag_2WO_4). has attracted increasing attention from scientists due to its several unique characteristics. Among them, we can cite its nontoxicity [1–3], photoluminescence properties [4,5], and photocatalytic applications [1–6]. These properties can be improved according to the obtained morphologies by different synthesis methodologies, such as simple co-precipitation [6–8], conventional hydrothermal [9,10], or microwave-assisted hydrothermal (MAH) method [11].

When it comes to time-saving synthesis, the MAH method is considerably more advantageous than other methodologies [12–15] since the use of microwave irradiation triggers different processes between the forming clusters and the electromagnetic waves, culminating in the formation of more oxygen defects and more structural/electronic disorder effects in the structure of the material [16].

* Corresponding authors.
E-mail addresses: mayaramondego.ufma@gmail.com (M.M. Teixeira), anacmora@gmail.com (A.C.M. Tello), elson.liec@gmail.com (E. Longo).
[1] These authors contributed equally to this work
[2] 0000-0001-9038-0024
[3] 0000-0001-5395-5650
[4] 0000-0003-4168-5774
[5] 0000-0003-4983-2695
[6] 0000-0002-5063-7603
[7] 0000-0002-6293-9393
[8] 0000-0001-9684-2568
[9] 0000-0002-3557-5555
[10] 0000-0001-6257-5537
[11] 0000-0003-0232-3957
[12] 0000-0001-8062-7791

https://doi.org/10.1016/j.jallcom.2022.163840
0925-8388/

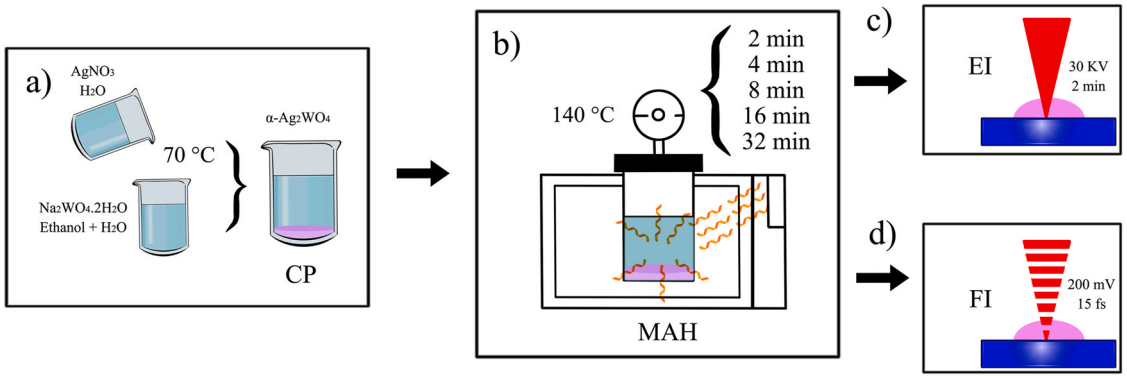

Fig. 1. Scheme with steps of a) Synthesis by CP method, b) Treatment by MAH method, c) Electron beam irradiation, and d) Femtosecond laser irradiation; to obtain α-Ag_2WO_4 samples.

The properties derived from the interaction between electromagnetic waves and the material have been studied for several decades. It is known that the characterization of structure or property responses of the material to these stimuli from the surrounding environment plays a key role in the understanding and rationalization of the structure-property relationship function in modern science and engineering [17,18]. In a recent study conducted by our group, α-Ag_2WO_4 was obtained by the MAH method. It was observed that the photoluminescence of these samples migrated from red to blue, according to the morphology and structural disorder presented [19].

It is also known that factors such as temperature, time of synthesis, and presence of surfactants among others can alter the lattice structural properties of α-Ag_2WO_4 as well [6,20,21]. Regarding the influence of time of exposure to MAH, in a recent study performed by Laier et al. (2020) [20] both experimental and computational results revealed that at certain times of operation of the MAH system it was possible to obtain samples with the highest active surface composition since they showed a higher density of broken bonds and greater surface energy. The irradiation of electron beam and femtosecond laser on the α-Ag_2WO_4 structure has attracted attention [10,11,22–32], where the main focus is to elucidate the mechanism of growth of Ag nanoparticles on the surface α-Ag_2WO_4 and the effects on the photoluminescence emissions [22,32–35].

In this work, we have tried to understand the phenomena provoked by the interaction between α-Ag_2WO_4 and electron beam and femtosecond laser irradiation, which were found to be able to promote changes in the lattice parameters, structure, and morphology of the crystal. All of these changes alter the material properties, for example, its electronic and magnetic properties, [22,34,35], photoluminescence emissions, and consequently its physical, chemical, and/or biological applications [6,20,31,36,37]. Therefore, it is possible to adjust the morphology, lattice, and electronic structures of α-Ag_2WO_4 materials resulting from these modifications [19,38].

It should be noted that alterations in the lattice structure of the crystal may directly contribute to the variation in the number of vacancies. Once there is a critical correlation among lattice parameters, structural stability, electronic structure, band gap, and photoluminescence properties, it is important to have a broad understanding at the atomic level of its bulk and surface.

In summary, this article came to increase knowledge about this structure and bring newness through the approach of explaining photoluminesce (PL), showing the surface that contributes to the property. It is well known that PL emission is the concentration of different defects: intrinsic (bulk and surface), extrinsic under interface, and structural order-disorder [32,39]. However, the surface contribution is still little known for the α-Ag_2WO_4 structure. For this purpose, we synthesized α-Ag_2WO_4 using the co-precipitation (CP) method, followed by the MAH method as a function of the synthesis time (2, 4, 8, 16, and 32 min) and electron beam and femtosecond laser irradiations. The crystals were characterized by different structural techniques, and their optical and PL properties were investigated. Theoretical calculations at the density functional theory (DFT) level were performed to obtain atomic information of the electronic structure of the material after irradiation. In addition, to understand the relationship between PL emissions of the α-Ag_2WO_4 exposed surfaces, the corresponding band gap was analyzed. The paper is organized as follows: Section 2 describes the experimental procedure (synthesis, characterization, and irradiation methods) and the theoretical method, whereas Section 3 shows the results and discussion on the structure, morphology, and optical properties of α-Ag_2WO_4. Finally, we present our main conclusions in Section 4.

2. Experimental section

2.1. Synthesis of α-Ag_2WO_4 crystals

The α-Ag_2WO_4 samples were synthesized by the CP method, similar to the description made by Foggi, et al. (2017) [40], being considered a volume of 30 mL of ethanol, then kept under continuous stirring for 10 min; the as-obtained sample was denoted as CP. The suspension followed by treatment in the MAH method (Fig. 1a,b) under the previous studies by [4,5,20,41], considering the treatment times of 2, 4, 8, 16, and 32 min. These samples were denoted as MAH-2, MAH-4, MAH-8, MAH-16, and MAH-32.

2.2. Irradiated samples (EI and FI)

To obtain the irradiated samples, the set of MAH samples were submitted to two different irradiations: electron beam irradiation (EI) (Fig. 1c) and femtosecond laser irradiation (FI) (Fig. 1d). The EI process was conducted in a field emission scanning electron microscope (Supra 35-VP; Carl Zeiss – Germany), using an acceleration voltage of 30 kV for 2 min, the parameters were selected based on experiments reported in the references [24,28,30]. The samples obtained through this process were denoted as EI-2, EI-4, EI-8, EI-16, and EI-32. Regarding the femtosecond laser irradiation, the procedure is according to Protocol I reported in reference [29], using a titanium/sapphire laser (Femtopower Compact Pro, Femto Lasers) with pulses of 30 fs of full width at half maximum, the wavelength of 800 nm, the repetition rate of 1 kHz and fluence of 60 J/cm^2 in diameter of the order of 20 μm. The obtained samples were denoted as FI-2, FI-4, FI-8, FI-16, and FI-32. Experimental characterizations of the samples are in Supplementary Information.

2.3. Model systems and theoretical methods

Density functional theory (DFT) calculations were performed with the CRYSTAL17 program [42]. The B3LYP hybrid functional [43] was used for described the electron-electron interactions combined with the effective core pseudopotentials (ECP) derived by Apra [44] and Corà [45] which have been chosen for described silver and tungsten, respectively, while the oxygen was described with the 8–411d11G basis set [46]. From the experimental results of Rietveld refinements of the CP sample, we derived a theoretical reference model (***opt*** – α-Ag_2WO_4) by full optimization of the structural parameters of α–Ag_2WO_4. The accuracy in the evaluation of the Coulomb and exchange was controlled by a set of tolerances with values of 10^{-8}, 10^{-8}, 10^{-8}, 10^{-8}, and 10^{-16}. A total mesh of 125 *k*-points was employed to sample uniformly the irreducible part of the Brillouin zone. The vibrational modes at the Γ point were calculated by using the numerical second derivates of the total energy. On the other hand, for the set of MAH, EI, and FI samples, only the atomic positions were allowed to relax. The relaxed structures were used for the electronic structure calculations. Visualization of the unit cells was performed using the VESTA program [47].

The electronic structure of the (010), (100), (001), (011), (101), and (110) surfaces of α-Ag_2WO_4 were discussed from band gap energy values and the density of states (DOS). Computational details for the calculations of the surface can be found in previous studies [48].

The density broken bonds in the α-Ag_2WO_4 surfaces were calculated as

$$D_b = N_b/A, \tag{1}$$

where N_b is the number of broken bonds and A is the surface area. The number of broken bonds for each surface was taken from reference [21].

The polyhedron energy band gap energy value for the morphologies of α–Ag_2WO_4 was calculated as follows

$$E_{ap}^{polyhedron} = \sum_i C_i \times E_{gap}^{surf} \tag{2}$$

where $C_i = A^{surf}/A^{polyedron}$ is the ratio of the surface area (A^{surf}) to the total surface area of the polyhedron ($A^{polyedron}$) and E_{gap}^{surf} is the energy value of the corresponding surface.

3. Results and discussion

3.1. Morphology

α–Ag_2WO_4 samples obtained by the CP method using 70% of water and 30% of ethanol, followed by treatment with MAH and exposure to EI and FI irradiations, were investigated by FE-SEM, as shown in Fig. S1 and Fig. 2. Through the CP method, only hexagonal rod-like morphologies were observed, with preferential growth on the y-axis in the (010) direction (Fig. S1). These characteristics were previously studied by our research group and are reported in reference [48]. In this method, the clusters of silver and tungsten ions solvated with water and ethanol interact randomly in a polarization process of complex clusters, depending on the moment of the permanent dipole of the neighboring clusters. This short-range interaction induces the first links between the crystal symmetry and its order/disorder. Then, to increase the symmetry and order of the crystal, there is a correlation between the rotation motions of permanent moments in the different complex clusters of silver and tungstate to form the different surfaces.

Theoretical calculations reported in the literature show that the morphological shapes of α–Ag_2WO_4 are formed by the combination of the (010), (100), (001), (110), (101), and (011) surfaces [21,48]. Although the theoretical results establish an ideal parallelepiped-like morphology for α–Ag_2WO_4, characterized by the presence of (010), (100), and (001) surfaces with predominant contributions of the (010) and (100) surfaces and a minor proportion of the (001) surface, experimentally a hexagonal rod-like morphology was observed (Fig. S1). Table 1 presents the values of E_{surf} according to R. A. Roca and et al. [48], as well as the surface band gap energy (E_{gap}^{surf}) and the percentage of contribution ($\%C_i$) for each morphology of α–Ag_2WO_4.

The experimental rod-like morphology of α–Ag_2WO_4 for the CP sample composed of the (010), (100), and (101) surfaces were obtained by destabilizing the E_{suf} of the (010), (110), and (100) surfaces from 0.20 to 1.44 Jm^{-2}, 0.65–1.50 Jm^{-2} and 0.38–0.70 Jm^{-2}, respectively, as well as by stabilizing the (101) and (001) surfaces from 0.68 to 0.23 Jm^{-2} and 0.53–0.22 Jm^{-2}, respectively (see Fig. 3).

In the MAH system, the monitoring of the experiment illustrated the time dependence in relation to the morphological evolution of α–Ag_2WO_4 (Fig. 2a-e). Morphologies composed of cube-like (highlighted in orange) and rod-like (indicated in blue) were observed in the samples treated with MAH at 2, 4, 8, and 16 min. Theoretically, the cube-like morphology composed of the (010), (100), and (001) surfaces can be obtained by stabilizing the (100) and (001) surfaces (Fig. 3).

At 32 min of treatment with MAH, a process of redissolution and stabilization of the (101) surface occurred, with concomitant destabilization of the (100) surface. This information allows us to understand how the time variation of the MAH treatment in an alcoholic environment influences particle growth. The microwave radiation induces a structural disorder through the modification of the bond distance, consequently altering the internal rotation barrier and vibration of molecules. In turn, the stabilization of previously unstable surfaces results in a new morphology [7,9]. Thus, at the highest synthesis time (32 min) the MAH-32 sample (Fig. 2e) presented no cubes – only rods behaving similarly to those obtained in the CP sample (Fig. S1). It is then believed that at a longer exposure time to microwave irradiation, the cube-like morphology is rearranged to a rod-like morphology.

It can be inferred that the microwave treatment directly interferes with the crystal morphology by either totally or partially dissolving the rod-liked crystals or altering the internal rotation movements between the clusters. Thus, in the MAH method, the cube-like morphology is formed by the less energetic surfaces, i.e., (100) and (001), with a decrease in disorder and an increase in symmetry (Fig. 3). The same behavior was observed in reference [28], in which the MAH method is employed to synthesize α-Ag_2WO_4 and different morphologies were obtained: hexagonal rod-like elongated, cubic-like, and triangular-like shapes.

Under electron beam irradiation, these morphologies change to a unique rod-like morphology (EI samples indicated by green color in Fig. 2f-j), whereas under femtosecond laser irradiation they change to the mixed rod- (violet color) and sphere-like morphologies (yellow color) (FI samples in Fig. 2k-o). The n-type semiconductor, α–Ag_2WO_4, when irradiated with electrons, grows on its surface metallic silver nanowires [10,11,30], thus forming silver vacancies inside the particle and causing a variation in the surface energies of the crystalline structure. Therefore, the value of the (101) surface drops from 0.68 to 0.23 Jm^{-2} (Fig. 3), becoming less energetic, while that of the (100) surface jumps from 0.38 to 0.70 Jm^{-2}, thus becoming more energetic. Even when varying the synthesis times, all samples exhibit agglomerated nature with characteristics similar to those observed in the CP sample (Fig. S1). In this micrograph, it can also be observed that the hexagonal rod-like morphology is better defined, with few imperfections. This fact can be considered an indication of the effect of electron beam irradiation on the morphology of α–Ag_2WO_4.

Under EI, the energy of the electron beam is transferred to the sample, causing different phenomena, such as atomic position

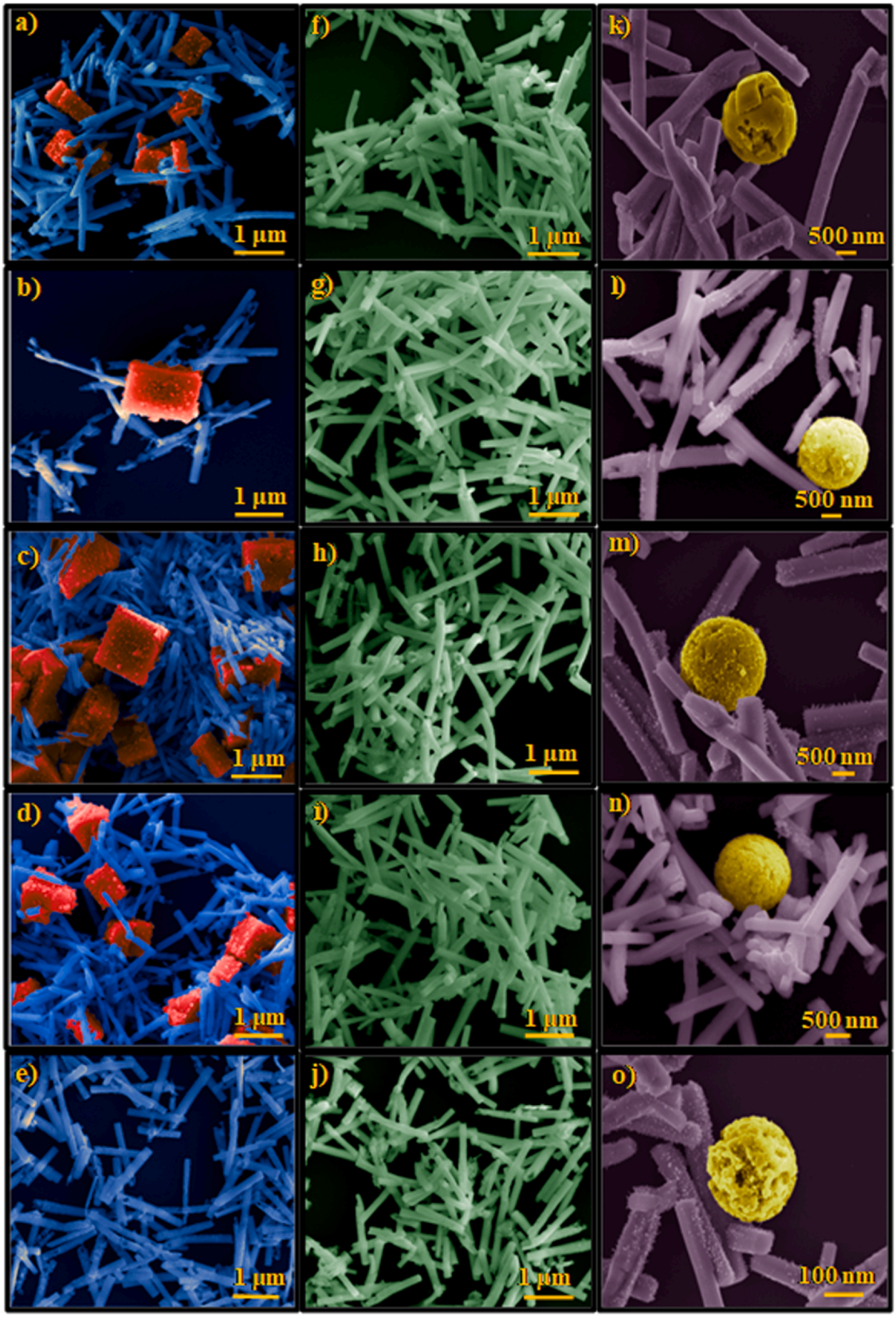

Fig. 2. FE-SEM images of α-Ag_2WO_4 particles of MAH, EI, and FI. a-e) heterogeneous morphology obtained after treatment with MAH at different treatment times (2, 4, 8, 16, and 32 min) with the cubes highlighted in orange color and the rods-like in blue color; f-j) rods-like with homogeneous morphology after EI indicated by green color; k-o) heterogeneous morphology of rods in violet color and spheres in yellow color after FI. (For interpretation of the references to colour in this figure, the reader is referred to the web version of this article.)

Table 1
Calculated density broken bond (D_b, nm^{-2}), surface energy (E_{surf}, Jm^{-2}), surface band gap (E_{gap}^{surf}, eV), percentage of contribution of each surface in the total area ($\%C_i$) and polyhedron band gap energy for the morphologies of α–Ag_2WO_4.

Morphology	Surface	D_b	E_{surf}	$\%C_i$	E_{gap}^{surf}	$E_{gap}^{polyhedron}$
Ideal α – Ag_2WO_4	(010)	4.68	0.20	52.5	1.39	0.99
	(100)	5.83	0.38	27.6	0.48	
	(001)	6.04	0.53	19.8	0.65	
Rod-like α – Ag_2WO_4	(010)	–	1.44	7.3	1.39	1.10
	(001)	–	0.22	13.2	0.65	
	(101)	8.75	0.23	79.4	1.15	
Cube-like α – Ag_2WO_4	(010)	–	0.20	42.9	1.39	0.92
	(100)	–	0.30	28.6	0.48	
	(001)	–	0.30	28.6	0.65	

change, surface distortions, electrostatic charge, and local heating in the crystals. Depending on the voltage and the type of sample, the electron beam will penetrate a few micrometers or nanometers deep into the sample. In our case, the voltage is 30 kV, whose penetration is in the order of nanometers, causing surface defects and atomic mobility that culminate in the formation of Ag nanoparticles on the surface of α-Ag_2WO_4 [11,49]. On the other hand, when a FI is applied, photons are absorbed by the sample to provoke excitation in the crystal system. To return to the ground state, the system segregates electrons, atoms, and ions from its structure, forming a plasma plume ablation, which is highly energetic. This plume interacts with the irradiated region, promoting energy exchanges, increasing temperature and pressure, accelerating the speed of movement of the species, and ejecting particles. After this highly energetic ablation process, the surface cools very quickly, which modifies the surface structure of the material [35,50].

Regarding the morphology obtained by the FI technique (Fig. 2k-o), it is possible to observe in α–Ag_2WO_4 spherical particles with well-defined edges and irregular extensions, in addition to elongated and slightly curved rods. According to the elementary mapping performed on the FI-8 sample (Fig. 4), both the spheres and the rods are composed of the same proportion of Ag, O, and W atoms, thus

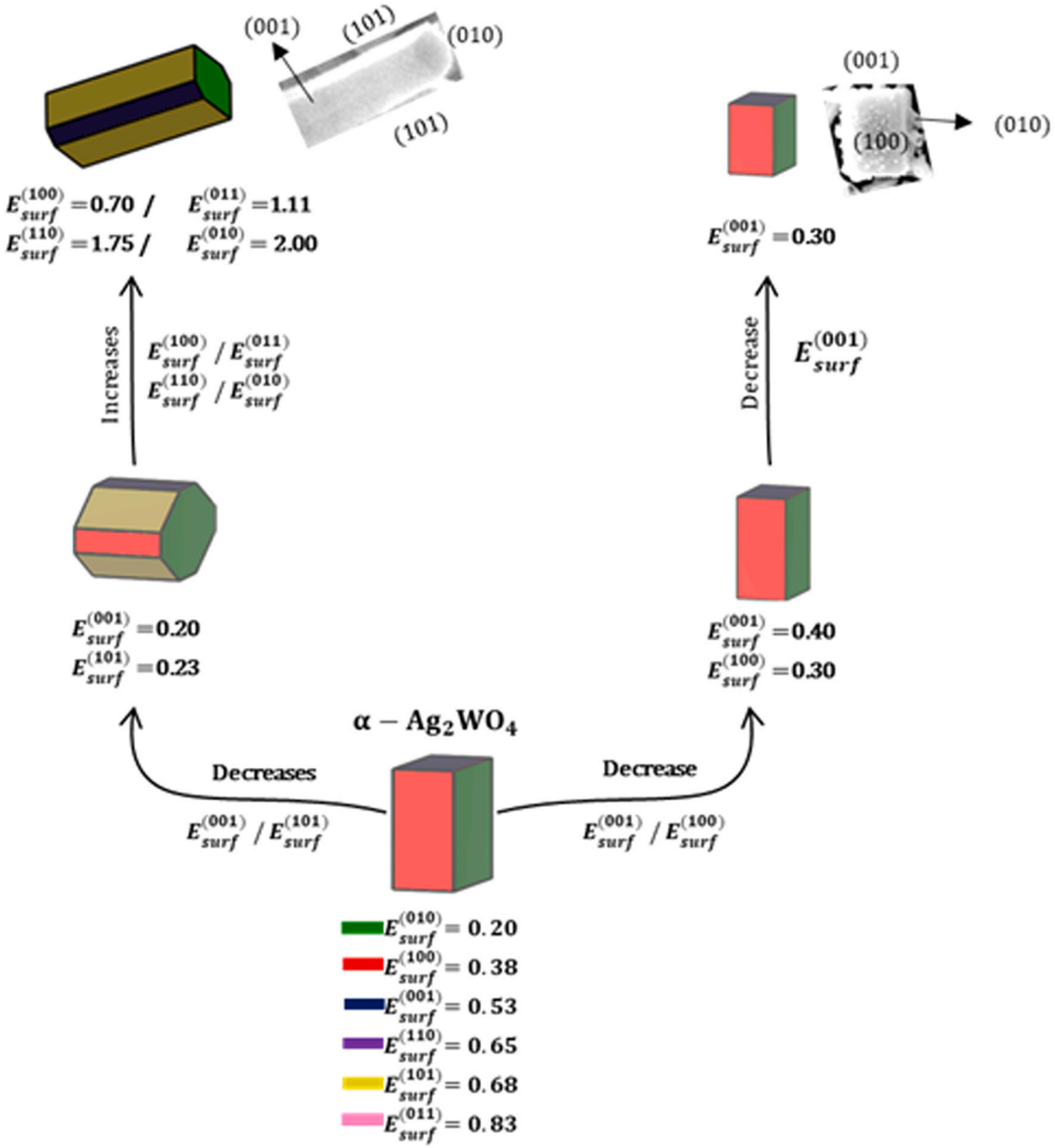

Fig. 3. Wulff construction for α–Ag_2WO_4. For comparison, experimental FE-SEM images are shown. E_{surf} values are given in Jm^{-2}.

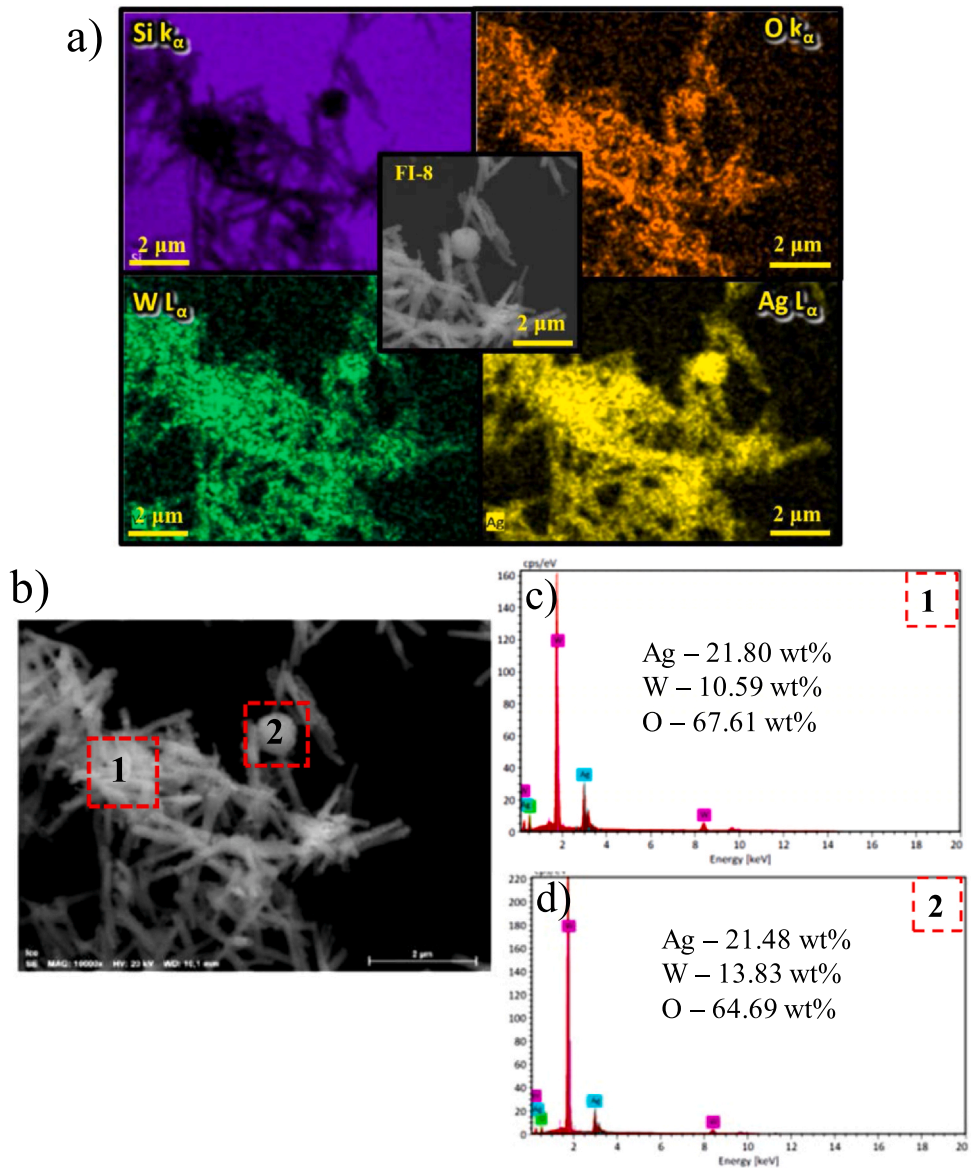

Fig. 4. a) EDS elemental mapping of the FI-8 sample of Si Kα, O Kα, W Lα, and Ag Lα. b) FI-8 sample analyzed by EDS, highlighting the rod- and sphere-like morphologies. c) Rod-like region 1 and d) Sphere-like region 2.

confirming the change in particle morphology composed of the same α–Ag_2WO_4 polymorph.

The application of the FI technique leads to the formation of a spherical morphology of α–Ag_2WO_4 powders due to when the femtosecond laser beam interacts with the α-Ag_2WO_4, a nonlinear and multiphoton ionization process occurs, which results in the formation of a plasma plume above the irradiated zone [31,51]. The highly energetic ablation process provokes the breaking of the bonds between the W—O and Ag—O atoms. Further, since the plasma itself can reach temperature and pressure values of up to 1000 K and 10^{12} Pa, respectively [51], such extreme conditions can trigger the sintering of the material that reminds in contact with the plasma. Since the plasma plume, which reaches values up to 1000 K, has a lifetime in the region of the ns [52], the plasma can transfer heat to the material surrounding the irradiation zone. Thus, the material that did not undergo sintering just experienced a melting process, resulting in the curvature of its edges. This effect is considered to favor the coalescence of the previously observed rods and cubes, giving rise to the morphology of the spheres.

The analysis in Fig. 2 suggests that in addition to the morphological changes already discussed, another relevant aspect is observed: the presence of silver nanoparticles on the surface of samples as a result of electron beam and femtosecond laser irradiations. This phenomenon has already been well discussed by our group [10,11,24,31,38–40]. These changes in sample morphologies allow us to understand how the surface structure can affect and modify the PL property of a semiconductor.

3.2. Unit cell and lattice parameters

The result of Rietveld refinement (Table S1) reveals that the lattice parameters and bond angle of all samples correspond to an orthorhombic structure and *Pn2n* spatial group, which is in agreement with the crystallographic information file in ICSD 4165 card [53]. Moreover, the R_{Bragg} and chi^2 fitting parameters evidence the accordance between the calculated data and the observed XRD patterns. The Rietveld refinement data show the effect of irradiation on the parameters of the unit cell, which were found to change. In general, when all MAH samples are irradiated by EI and FI, there is

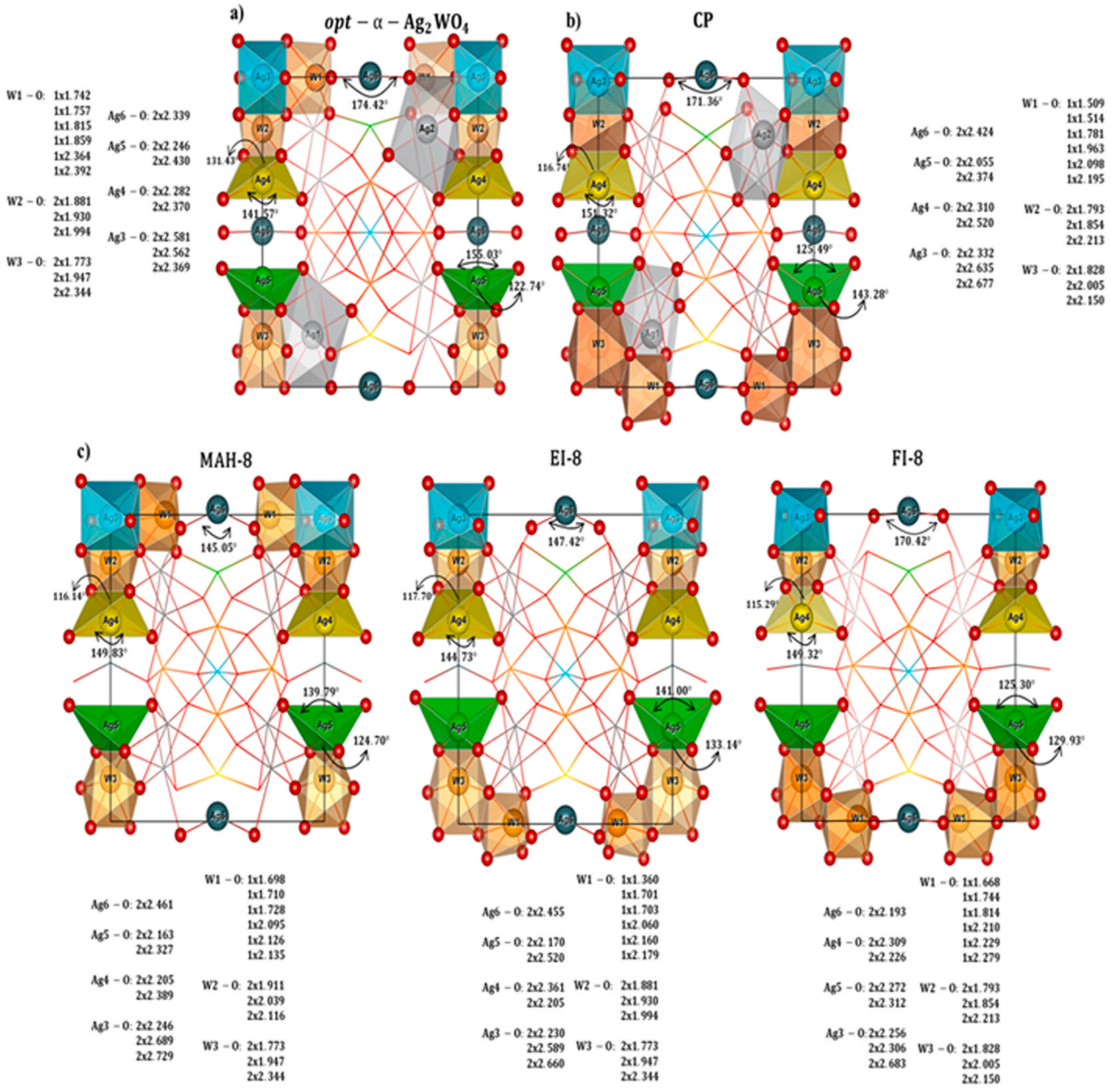

Fig. 5. The geometry of a) opt – α-Ag_2WO_4, b) CP, and c) irradiated (MAH-8, EI-8, and FI-8) structures.

an expansion in the cell volume, consequently altering the lattice of the samples.

Fig. 5 brings a comparison among the geometries for optimized (*opt*—α-AWO), neutral (CP), and irradiated structures (MAH-8, EI-8, and FI-8). From this figure, it is possible to observe variations of the relative positions of the Ag, O, and W atoms on several different constituents $[WO_6]/[AgO_y]$ clusters (y = 7, 6, 4, and 2) of α–Ag_2WO_4. Since the $[AgO_2]$ and $[AgO_4]$ clusters are found in the shell of the unit cell, changes are expected as a result of the strong interaction caused by irradiation, leading to nucleation and formation of metallic Ag [24,25]. Thus, the comparison between the *opt*—α-AWO geometries and MAH-8 structures for the sample treated with MAH indicates variations in the Ag—O distances and O—Ag—O angles, mainly in the $[AgO_2]$ and $[AgO_4]$ clusters. In the $[AgO_2]$ cluster, Ag—O increases from 2.246 to 2.461 Å, while O—Ag—O decreases from 174.42 to 145.05 º. In the case of the Ag—O bond in $[AgO_4]$ clusters, an increase in two bond distances is observed. When the MAH-8 sample is exposed to EI, both Ag—O distance and O—Ag—O angle in the $[AgO_2]$ cluster remain almost unchanged, going from 2.461 to 2.455 Å and from 145.05 to 147.42 º, respectively, whereas the Ag—O distance in the $[AgO_4]$ clusters undergoes increases. On the other hand, when a femtosecond laser is applied, the Ag—O distance in the $[AgO_2]$ cluster decreases from 2.461 to 2.193 Å, while the O—Ag—O angle increases from 145.05 to 170.42 º. Regarding the $[AgO_4]$ clusters, it is possible to note a shortening average of the Ag—O distance. With respect to the different types of $[WO_6]$ clusters, in all cases, the W—O bond distances of the irradiated samples undergo variations corresponding to W1, in which an average lengthening is observed.

A careful analysis of the Ag—O and W—O bond distances for all samples were performed, and the observed values are listed in Table S2.

From Fig. 5 and the values in Table S2, we can infer that the MAH treatment induces a larger structural organization in the α–Ag_2WO_4, which is evidenced through the average lengthening of the Ag–O and W–O bonds in the $[WO_6]/[AgO_y]$ clusters (y = 7, 6, 4, and 2). Considering the EI, it can be noted that the irradiation with electrons

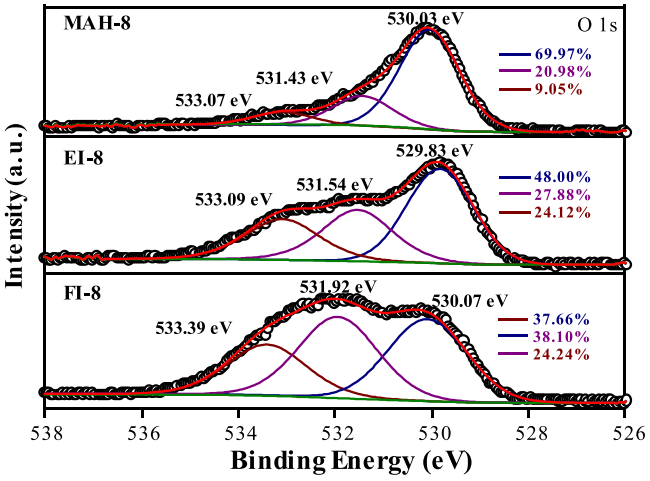

Fig. 6. High-resolution XPS spectra of O 1 s for the MAH-8, EI-8, and FI-8 samples.

leads to structural changes in the [AgO_4] and [$W1O_6$] clusters. On the other hand, FI induces an average shortening of Ag–O and an average lengthening of W1–O bond distances in the clusters of α–Ag_2WO_4 when compared with both MAH samples and the optimized system. These results explain the constant changes in the crystal lattice and the size reduction of [AgO_y] clusters proposed by our group [22], which may also be induced by rod-to-sphere morphology changes in the irradiated samples.

To investigate the effect of irradiation on the particle surface, XPS measurements were conducted. Such analyses were performed in the samples that had their morphology and the PL property changed, that is, MAH-8, EI-8, and FI-8.

Fig. 6 shows the high-resolution spectra of O *1s*, which were fitted with three components. The strong peak around 530.03 eV, 529.83 eV, and 530.07 eV for the MAH-8, EI-8, and FI-8 samples, respectively, are attributed to the O atom in the α-Ag_2WO_4 lattice. The peak at 531.43 eV, 531.54 eV, and 531.92 eV, respectively, are assigned to oxygen defects in the lattice, such as oxygen vacancies (V_O) [54]. Lastly, the peak in the high binding energy, i.e., above 533 eV, is related to adsorbed oxygen on the surface [54,55].

Changes in the profile of the high-resolution spectrum of O *1 s* indicate a high percentage of adsorbed oxygen on the surface of the EI-8 and FI-8 samples in comparison with MAH-8. Additionally, there is a decrease in the area percentage of the lattice oxygen to 69.97% for MAH-8, 48.00% for EI-8%, and 37.66% for FI-8, as well as an increase in the area percentage ascribed to defect oxygen to 20.98%, 27.88% and 38.10% for the MAH, EI and FI samples, respectively. This indicates a possible formation of oxygen vacancies in the EI and FI samples. The vacancies formed are a charge compensation due to destabilization of the (010) surface along the transformation of morphology from cubes-like into rods-like.

Furthermore, surfaces can be stabilized by reducing surface charge density via different mechanisms: creating surface states, redistributing charge between atoms, removing atoms, adding charged impurities to the surface, or creating faces [56,57]. In the process of electron beam and femtosecond laser irradiations, we observed the destabilization of the surface (010), by the conversion of cubic particles into rods, which was compensated by the removal of surface oxygen atoms and by chemoadsorption of species (O^- and O^{2-}) on the surface, according to the XPS results.

The increment in oxygen vacancies and impurities, via FI, may be related to the fact that the experiment is carried out in an environment, which allows the exchange of charges and species. It is known that the greater exposure of a given crystalline surface influences the properties of materials [58]. An analysis of the theoretical results renders that the (010) surface presents the highest value of surface energy in the rod morphology. Extrapolating this data to the literature [58], we suppose that to compensate for the energetic instability, superficial oxygen vacancies were created.

Fig. S2a shows that the Ag *3d* spectra were better fitted using one component. The high-intensity peaks located at approximately 368 eV and 374 eV are related to the $3d_{5/2}$ and $3d_{3/2}$ orbitals, respectively, with Ag^+ binding energy. No significant changes were observed among the spectra of the samples.

The XPS technique also provided information on the chemical environment of the W element, which is considered to be the lattice-forming atom. Fig. S2b displays the XPS spectra of the W *4 f* for the MAH-8, EI-8, and FI-8 samples. The binding energy corresponds to the $4f_{7/2}$ and $4f_{5/2}$ orbitals of W^{6+} in the α–Ag_2WO_4 lattice [4,59,60]. The XPS spectra reveal a similar profile in all samples, with no changes in the oxidation state or chemical environment of the structural W atom, nor even for the EI and FI samples. Therefore, it can be concluded that the irradiation process changes the environment around oxygen atoms due to the formation of metallic Ag and V_O vacancies, consequently leading to distortions in the angle and bond distance of the Ag and W clusters (Table S2).

3.3. Structural characterization

Fig. S3 displays the Raman spectra in the range of 60–960 cm^{-1} at room temperature. According to Turkovič et al. (1977) [61], there are 21 known Raman modes for α-Ag_2WO_4 ($6A_{1\,g}$, $5A_{2\,g}$, $5B_{1\,g}$, and $5B_{2\,g}$). As it can be observed in Figs. S3a-d, six Raman modes were detected for all samples ($1A_{1\,g}$, $1A_{2\,g}$, $3B_{1\,g}$, and $1B_{2\,g}$); the remaining modes were not detectable experimentally because of their low intensities. External vibrational modes of interaction between silver and tungstate ion and [AgO_y] (y = 7, 6, 4, 2) clusters can be identified between 100 and 500 cm^{-1}, whereas internal vibrational modes assigned to the vibrations in the [WO_6] clusters can be detected between 500 and 1000 cm^{-1} [28,37,62]. It is possible to observe in both materials two intense bands: one at 102 cm^{-1}, attributed to the stretching of T′(Ag^+/W^{6+}) binding [63], and another at 877 cm^{-1}, assigned to the symmetrical stretching of the W—O bond in the octahedral [WO_6] cluster [28].

The comparison between the relative experimental and theoretical positions of these vibrational modes is illustrated in Fig. S3e and summarized in Table S3, confirming the good agreement between the experimental and theoretical modes.

Following the Raman discussion on the short-range structural disorder, XANES allowed us to visualize a local disorder, which in our case was around the tungsten atom. In the past decade, our research group has employed the XANES technique to study the local structure of various semiconducting metal oxides, such as tungstates, titanates, and vanadates among others [19,64–68].

Herein, we performed XANES measurements to investigate the effect of irradiation on the local structure around W atoms. Fig. S4a displays the W-L1 XANES spectra of the as-prepared CP sample and some standards used as reference samples (Na_2WO_4, WO_2, and monoclinic WO_3). In Fig. S4a, it is possible to observe a pronounced peak (here denoted as P1) in the Na_2WO_4 spectrum, more specifically in the pre-edge region, as well as a shoulder in the m-WO_3 standard and the CP sample spectra. The physical origin of such electronic transition (peak P1) is described elsewhere [19,69,70].

It is well established that an intense pre-peak in the W-L1 edge XANES spectrum has been found in materials constituted by tetrahedral units (WO_4), such as the Na_2WO_4 compound [5,70]. The electronic transition responsible for P1 pre-peak is forbidden in the materials that exhibit regular [WO_6] units. However, compounds presenting non-regular octahedral symmetry (distorted WO_6 clusters) have been found to present a less intense pre-peak similar to that in the WO_3 spectrum [69,70]. From the analysis of the spectrum of the CP sample, it is possible to observe its similarity with the WO_3

standard spectrum. It is then plausible to affirm the presence of distorted [WO_6] clusters in the as-prepared CP sample. Furthermore, by comparing the spectra of the α–Ag_2WO_4 samples (Fig. S4b) it is evident the similarity with the XANES spectra (both in the pre- and post-edge regions). Such behavior reveals that the microwave-assisted hydrothermal treatment, as well as the irradiation processes (EI and FI), resulted in samples constituted by distorted octahedral WO_6 clusters.

3.4. Density of states

The experimental optical band gap was estimated using the Wood-Tauc relation [71,72] and the Kubelka-Munk equation [72,73], evidencing a slight variation from 3.09 to 3.32 eV (Fig. S5) for the MAH, EI, and FI samples. The experimental results show that when the CP sample is submitted to MAH treatment for 2 min, the band gap value decreases from 3.13 eV to 3.08 eV. In contrast, for the MAH-4, MAH-8, MAH-16, and MAH-32 samples, the band gap increases. Later, when these samples are under EI, is observed that except for the EI-2 sample, the band gap decrease in all cases. For the FI-2 and FI-4 samples present an increase in the band gap, while for the FI-8, FI-16, and FI-32 samples, an opposite effect can be sensed. Structural order-disorder effects induced by the radiation as well as the morphology, time process, and shape powder can explain the band gap decrease/increase of α-Ag_2WO_4.

The electronic structure of α-Ag_2WO_4 was analyzed from the partial density of states (PDOS) of the *4d*, *5d,* and *2p* orbitals of Ag, W, and O atoms, respectively (Fig. 7), where the valence band maximum (VBM) is set to zero. In terms of contributing states, the representation is similar for all samples, according to the composition of the valence band (VB) and conduction band (CB) of the different samples. As already known, for α–Ag_2WO_4 the VB is formed by the hybridization of $4d_{xy}$ and O $2p_z$ orbitals, whereas the bottom of the CB is mainly composed of W *5d* orbitals, more specifically $5d_z{}^2$ orbitals. However, differences in topology occur among the PDOS of neutral and irradiated samples. In the PDOS of the neutral sample, there is discontinuation in the VB, leading to two distinct Ag *4d* blocks. Such characteristic is maintained in the EI-8 sample, while in the PDOS of the MAH-8 and FI-8 samples the double-peak structure disappears.

In the MAH-8 and FI-8 samples (Fig. 7**c**), localized states of the O $2p_x$, $2p_y$, and $2p_z$ and Ag $4d_{xy}$ orbitals are evidenced in the Fermi region, as well as localized $5d_{x^2-y^2}$ and $5d_z{}^2$ orbitals forming the bottom of the CB in these samples. The localized density of O *2p* and W *5d* states situated at the Fermi level and the bottom of the CB, respectively, favors the electronic transfer from the O *2p* to W *5d* states, which are necessary for the excitation process of the tungstate groups. These observations in the electronic properties of the different samples are associated with the structural disorder induced by the irradiation in the α–Ag_2WO_4 lattice, as seen in Fig. 5.

Fig. 8 shows the PL spectra of α–Ag_2WO_4 samples measured at room temperature and excited at 355 nm. The PL spectra encompass the whole visible region and part of the near-infrared region, presenting a broadband profile. The small changes in the profile of the PL spectrum between the same group are related to different degrees of order/disorder in the O–Ag and O–W bond lengths. Therefore, by analyzing the PL spectra we can understand how the MAH treatment time, and electron beam and femtosecond laser irradiations affect the emission spectrum of α–Ag_2WO_4.

The CP and EI samples with rod-like morphology (Fig. S2 and Fig. 2f-j) have two maximum emission centers: around the green (550 nm) and the red (733 nm) regions (Fig. 8a,b). The FI sample with rod- and sphere-like morphologies presented the same emission centers (Fig. 2k-o and Fig. 8c). When the sample is submitted to MAH at synthesis times between 2 and 16 min, two types of morphologies are observed (rod- and cube-like, Fig. 2a-d), and the maximum emission center around 550 nm is favored (Fig. 8a). However, the sample treated with MAH at a prolonged synthesis time of 32 min, in addition to only hexagonal rod-like particle morphology, presents two maximum emission centers similar to those of the CP sample.

It is well known that the PL property of α–Ag_2WO_4 is strongly correlated by photogenerated electron-hole pair processes and in terms of the electronic transition between the VB (*2p* levels of oxygen atoms and *4d* level of silver atoms) and the CB (*5d* levels of tungsten atoms) as well as the contribution of intermediate levels between the VB and CB [22,32,33,66,74].

The blue band is attributed to the radiative transition from the O_{2p} states to the W_{5d} states while the green band is due to the electronic transition from the Ag^+–V_O defects level to the VB [62]. Blue/Green emission was also related to distorted [WO_6] octahedral, while red emission to the [AgO_y] (y = 2, 4, 6, and 7) clusters that form complex vacancies, inducing more disorder and deeper defects in the forbidden band gap [32,38,75].

Furthermore, the [AgO_y] (y = 2, 4, 6, and 7) and [WO_6] clusters in pairs have extrinsic defects, which are linked to order-disorder effects in the electronic structure, surface, and interfaces, which create additional energy states above the VB and below the CB, which decrease the band gap [32,66]. However, a specific assignment of surface and the clusters that are present on each surface that contributes to PL emission has not been observed. Here, we can observe the influence of particle morphology and surface band gap since the distortions in the lattice favor different distributions of electronic state in the surface (Fig. 9).

To analyze the difference between the emission spectrum and the contribution of each surface (Fig. 9), a comparison among the MAH-8, EI-8, and FI-8 samples with the cube-, rod- and sphere-like morphologies, respectively, is presented in Fig. 10. Since each of the surfaces of α–Ag_2WO_4 presents a different band gap energy (E_{gap}^{surf}) value, it is expected that each surface has a specific contribution in the PL property. This can be justified by the fact that each surface is quite different in terms of the coordination number of atoms, the distance between adjacent atoms, and available electron density [22,30].

The theoretical E_{gap} values of surfaces and the rod- and cube-like morphologies of α–Ag_2WO_4 are listed in Table 1**.** According to the results, all surfaces studied show E_{gap}^{surf} values reduced in comparison to the E_{gap} value of the bulk. The density of defects on the surface can justify the existence of intermediary states in the band region of the bulk, which come from the number of Ag–O and W–O bonds that are broken when a slab surface is created. To quantify the defects on the surface, the density of broken bonds was calculated as , where N_b is the number of broken bonds and A is the surface area. The results corroborate that those surfaces with higher D_b values present the lowest band gap (Table 1) and consequently, intermediary states (Fig. 9).

Regarding the $E_{gap}^{polyhedron}$ for each experimental morphology, the results reveal that in passing from ideal to the experimental rod-like morphology, the $E_{gap}^{polyhedron}$ value increase from 0.99 eV to 1.10 eV due to the appearance of the (101) surface which comes to dominate the Wulff construction (79.4%) for the rod-like morphology and has a band gap of 1.15 eV. The (010) and (001) surfaces are also exposed in this morphology in a lower proportion (7.3% and 13.2%, respectively). In the case of the passing from ideal to the experimental cube-like morphology, the $E_{gap}^{polyhedron}$ decrease from 0.99 eV to 0.92 eV at the time that (001) and (100) surfaces that have the lower band gap values 0.65 eV and 0.48 eV, respectively, increase their contribution (28.6% each one) to the cube-like morphology that exposed the (010) surface (42.9%) which have band gap (1.39 eV).

It is worth nothing that theoretical values of band gap energy are not the same that those obtained experimentally because the

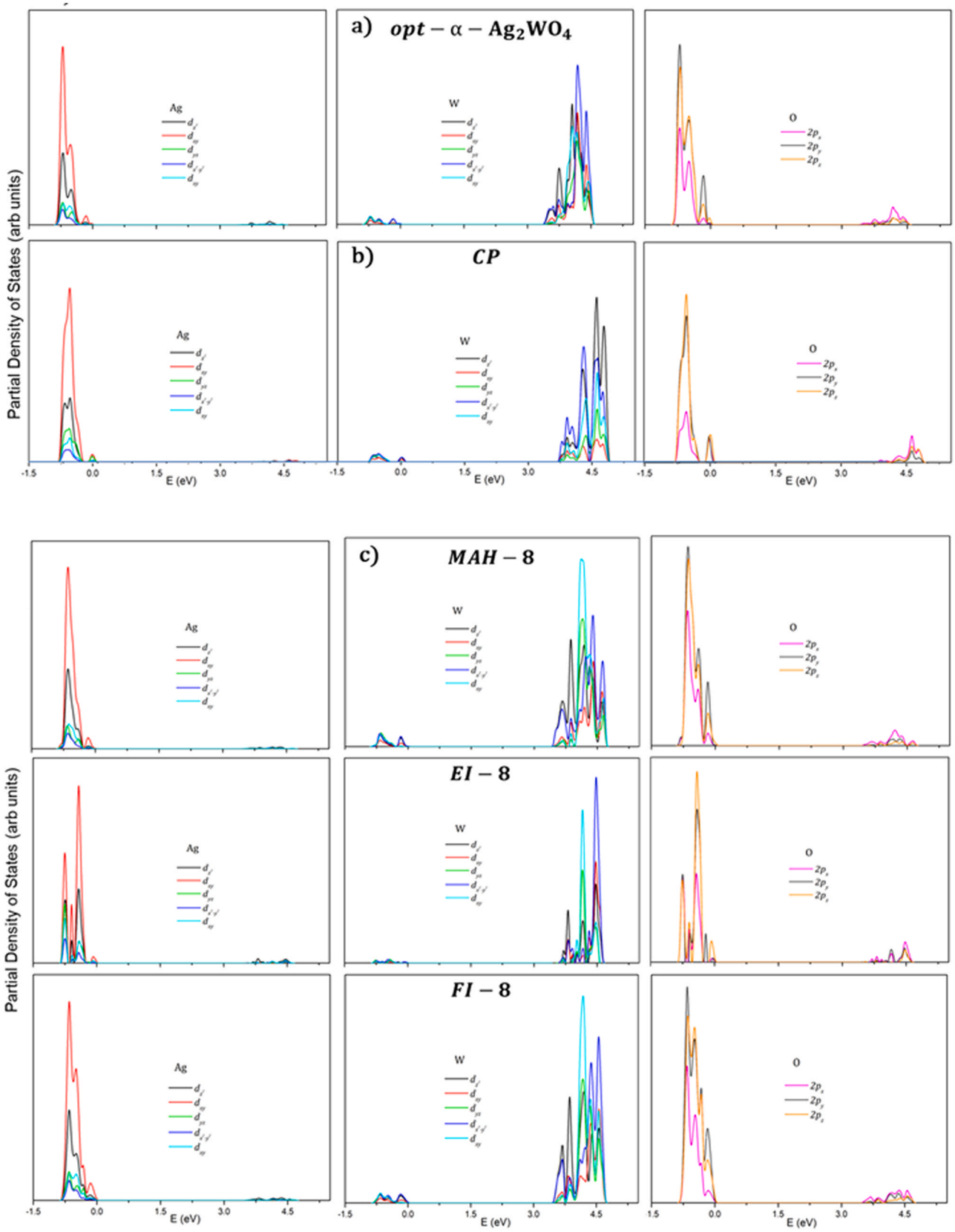

Fig. 7. Partial density of states projected on the *4d*, *5d*, and *2p* orbitals of Ag, W, and O atoms, respectively, for a) *opt*–α-Ag_2WO_4, b) CP, and c) irradiated (MAH-8, EI-8, and FI-8) samples.

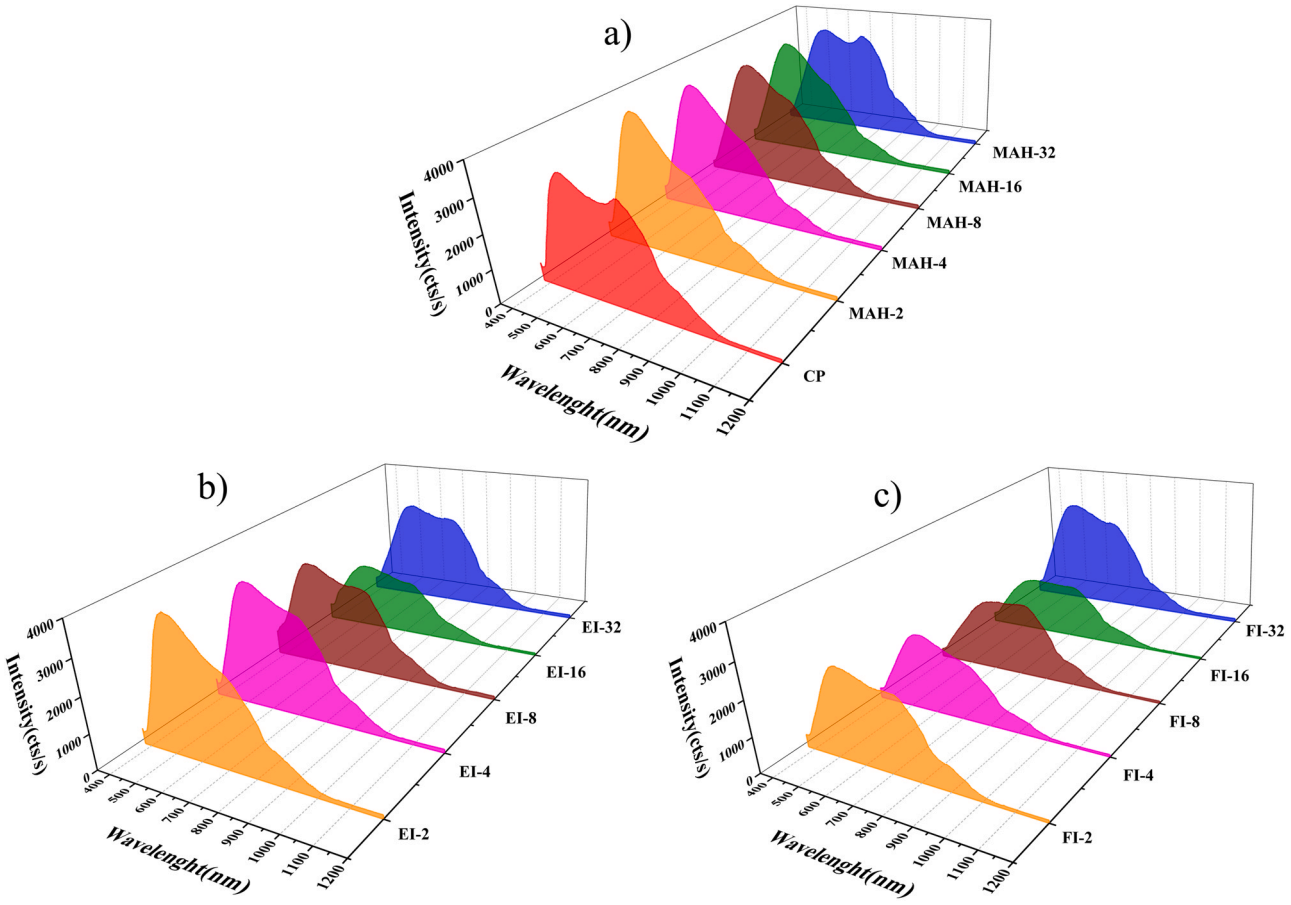

Fig. 8. PL spectra of the samples obtained by a) the CP method, treated with MAH, and irradiated by b) EI and c) FI.

experimental techniques used for such measurements considering the effect bulk/surface of the material and in the calculations have been considered only the exposed surface structures at the morphology.

Fig. 10**a** shows that both CP and EI-8 samples are composed only of rod-like morphologies. The PL spectrum for the CP and EI-8 samples showed two maximum emission centers – around 550 nm

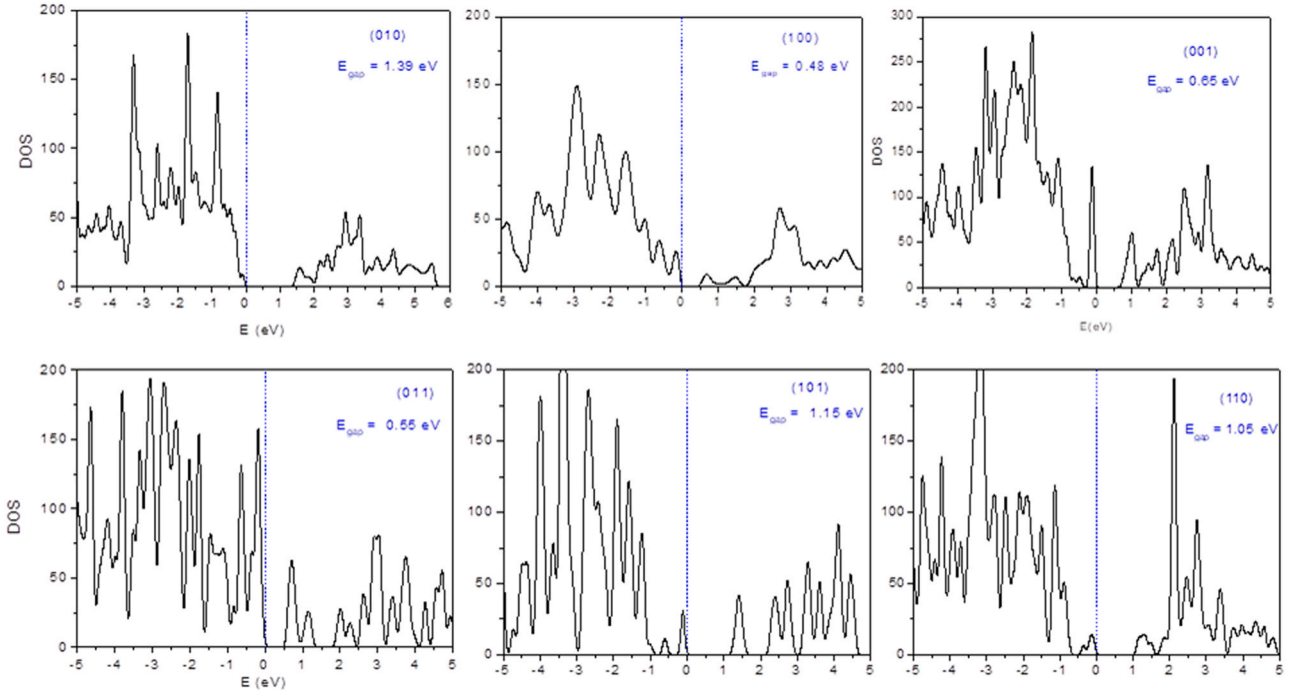

Fig. 9. The total density of states for the (010), (100), (001), (011), (101), and (110) surfaces of α-Ag_2WO_4.

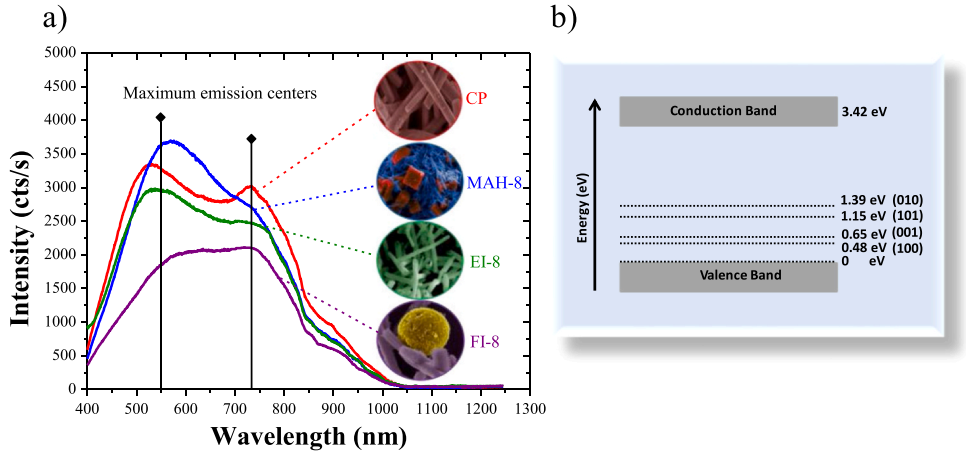

Fig. 10. a) PL spectra and maximum emission centers of the CP, MAH-8, EI-8, and FI-8 samples. b) Comparative diagram of the band gap value of the optimized structure (3.42 eV) and band gap values for (100), (010), (001), and (101) surfaces.

and 733 nm – regions. In the case of the MAH-8 sample, it is composed of both cube- and rod-like morphologies and although the PL spectrum also present two emission centers, is observed that the maximum emission center around 550 nm is favored while the emission center is 733 nm present intensity lower. Finally, the sample irradiated by femtosecond laser (FI-8) with rod- and sphere-like morphologies presented an equilibrium in the maximum emission centers with a slight shift to the red region. Based on these results, we can conclude that (010) and (101) surfaces contribute to the emission centers at 550 nm and 733 nm, respectively.

As previously mentioned, (010) surface has the highest band gap, therefore it tends to contribute to the highest energies emission (Fig. 10b), in addition, is present in both morphologies, see Table 1, and is the aim component of the cube-like morphology, thus, the presence of both cube- and rod-like morphologies in the sample contributed to the emission to 550 nm. In contrast, (101) surface is the main component of the rod-like morphology, and therefore the sample only with rod shows a defined emission at 733 nm. The highest intensity of emission in 550 nm is associated with the presence of localized states in the forbidden band gap due to (010) surface, see Fig. 9 and Fig. 10b, which favored the probability of the transition in this surface.

As has been established in the (101) surface are present distorted $[WO_6]_d$ cluster, and the under-coordinated $[AgO_5{\cdot}2V_O^x]$, $[AgO_4{\cdot}3V_O^x]$, and $[WO_5{\cdot}V_O^x]$ clusters. The complete distorted $[WO_6]_d$ clusters are considered as a source of electrons due to while the under coordinated $[AgO_5{\cdot}2V_O^x]$, $[AgO_4{\cdot}3V_O^x]$ clusters, and $[WO_5{\cdot}V_O^x]$ clusters supporting charge positive are considered a source of the hole [76,77].

In the case of the (010) surface complete distorted $[WO_6]_d$ and $[AgO_4]_d$ clusters present in the surface are a source of electrons while under-coordinated $[AgO_5{\cdot}2V_O^x]$ clusters are a source of holes. Thus, the transfer electron-hole occur from complete distorted clusters to under-coordinated $[AgO_5{\cdot}2V_O^x]$ clusters, the above also explain the contribution of the (010) surface to the PL property [21].

Moreover, the cube- and rod-like morphologies have a stable (001) surface, which has the E_{gap}^{surf} (0.65 eV), see Table 1 and Fig. 10b. The (001) surface has a percentage of total area contribution in both morphologies of 28.6% and 13.2%, respectively. The (001) surface has $[WO_5{\cdot}V_O^x]$, $[AgO_5{\cdot}2V_O^x]$, $[AgO_4{\cdot}3V_O^x]$, and $[AgO_4{\cdot}2V_O^x]$ clusters [21]. The cube-like morphology also has a stable (100) surface, which has the lowest E_{gap}^{surf} (0.48 eV), Fig. 10b. The (100) surface has $[WO_4{\cdot}2V_O^x]$, and two $[AgO_5{\cdot}2V_O^x]$ clusters [21].

In general, the samples with cube-like morphologies showed a maximum center emission in the green region, while those with particles with only rod-like morphology showed two maximum emission centers (in the green and red regions). Differently, the sphere-like morphology presented an equilibrium in the emission centers. The PL behavior demonstrates the influence of many factors, such as the orientation between particles, the variations in the particles size distribution, the morphology of the particles, and surface defects [32].

The XYZ color space created by the International Commission on Illumination (abbreviated as CIE) serves as a standard reference to represent the color emitted by the materials, and this color is expressed by a resulting chromaticity symbolized by the coordinates (x, y) [62]. The chromaticity coordinates x and y under excitation of 355 nm were obtained in the CIE XYZ color space (Fig. S6), and the detailed information is shown in Table S4.

The MAH group revealed variation in their color from orange to red (Fig. S6a) due to the synthesis time, which disorganized the $[AgO_y]$ clusters. The CIE diagram of the EI and FI groups also showed a color variation from orange to red (Fig. S6b). Among the samples submitted to femtosecond laser irradiation, the FI-32 was found to be the most resistant to the laser action, remaining practically unchanged when compared to the MAH-32 (Fig. S6c and Table S4). The other samples migrated from orange to red, following what was observed for samples irradiated by electrons. Therefore, the PL measurements demonstrated that microwave, electron beam, and femtosecond laser irradiations altered the electronic density of the bulk and surface since the behavior of the samples changed after irradiation. However, the sample obtained at the longest synthesis time did not show variation in the density of V_{Ag} and V_O vacancies when subjected to electron or femtosecond irradiation, which is possibly related to its more stable rod-like morphology.

4. Conclusion

In summary, in this work, we discussed the influence of morphology, surface band gap, and microstructure on the PL property of α–Ag_2WO_4 samples obtained by the CP method, followed by treatment with MAH at different synthesis times and two different irradiation processes: electron beam and femtosecond laser. The experimental and theoretical study clarifies the important relationship between the DOS of different surfaces and the PL property. It was observed that the use of different ways of treating the samples successfully changed the surface characteristics, microstructure, and electronic density of the α–Ag_2WO_4 materials. Electron beam and femtosecond laser irradiations were found to cause expansion of the unit cell, form oxygen vacancies on the surface, change the angle and distance between O–Ag and O–W bonds, and modify the particle morphology to rod-, cube- and sphere-like. The theoretical calculations showed how changes in the microstructure, morphology, and

surface band gap values can alter the distribution of electron density, and consequently the emission centers. Cube-like morphology shows a high contribution of the (010) surface, while rod-like morphologies showed the contribution of (010) surface and (101) surface. Moreover, the sample submitted to a longer synthesis time of 32 min in the microwave system presented the most stable rod-like morphology and high resistance to the disorder of the network-modifying [AgO_y] clusters. Therefore, the more ordered the network-forming [WO_6] clusters, the more difficult it will be to introduce defects. For this reason, no significant changes were observed in the PL property. These results enrich the literature regarding the effect of different techniques associated with microstructure, morphology, and band gap energies on the PL properties of semiconductor materials.

CRediT authorship contribution statement

Mayara Mondego Teixeira: Conceptualization, Methodology, Formal analysis, Investigation, Roles/Writing – original draft. **Lílian Cruz Santos:** Conceptualization, Methodology, Formal analysis, Investigation, Writing – original draft. **Ana Cristina Mora Tello:** Conceptualization, Methodology, Formal analysis, Investigation, Writing – original draft. **Priscila Barros Almeida:** Conceptualization, Methodology, Formal analysis, Investigation, Writing – original draft., **Jussara Soares da Silva:** Conceptualization, Methodology, Formal analysis, Investigation, Writing – original draft. **Letícia Laier:** Conceptualization, Methodology, Formal analysis, Investigation, Writing – original draft. **Lourdes Gracia:** Formal analysis, Resources, Supervision. **Marcio Daldin Teodoro:** Formal analysis, Visualization, Writing – original draft preparation. **Luís Fernando da Silva:** Formal analysis, Visualization, Writing – original draft preparation. **Juan Andrés:** Conceptualization, Investigation, Supervision, Writing – review & editing. **Elson Longo:** Conceptualization, Data Curation, Formal analyses, Project administration, Resources, Supervision, Visualization, Writing – review & editing.

Declaration of Competing Interest

The authors declare no competing financial interest.

Acknowledgments

The authors are grateful for the support of the Brazilian research financing institution: Coordenação de Aperfeiçoamento de Pessoal de Nível Superior - Brazil (CAPES) - Finance Code 001, Conselho Nacional de Desenvolvimento Científico e Tecnológico - (CNPq) Brazil, and Fundação de Amparo à Pesquisa do Estado de São Paulo - (FAPESP) Brazil-(CDMF, Proc.2013/07296–2). J. A. acknowledges Universitat Jaume I (Spain) for project UJI-B2019-30, and Ministerio de Ciencia, Innovación y Universidades (Spain) project PGC2018-094417-B-I00 for supporting this research financially. This research was partially performed at the LNLS (project XAFS2–20180338), Campinas, SP, Brazil. The authors acknowledge Dr. Gladys Miguez-Vega for the femtosecond laser irradiation measurements.

Appendix A. Supporting information

Supplementary data associated with this article can be found in the online version at doi:10.1016/j.jallcom.2022.163840.

References

[1] Y. Li, Y. Li, S. Ma, P. Wang, Q. Hou, J. Han, S. Zhan, Efficient water disinfection with Ag2WO4-doped mesoporous g-C3N4 under visible light, J. Hazard. Mater. 338 (2017) 33–46, https://doi.org/10.1016/j.jhazmat.2017.05.011

[2] M. Pirhashemi, A. Habibi-Yangjeh, Preparation of novel nanocomposites by deposition of Ag2WO4 and AgI over ZnO particles: efficient plasmonic visible-light-driven photocatalysts through a cascade mechanism, Ceram. Int. 43 (2017) 13447–13460, https://doi.org/10.1016/j.ceramint.2017.07.049

[3] Y. Li, B. Zhu, J. Yu, W. Ho, P. Xia, Fabrication and photocatalytic activity enhanced mechanism of direct Z-scheme g-C3 N4 /Ag2WO4 photocatalyst, Appl. Surf. Sci. 391 (2016) 175–183, https://doi.org/10.1016/j.apsusc.2016.07.104

[4] H. Li, Y. Zhou, L. Chen, W. Luo, Q. Xu, X. Wang, M. Xiao, Z. Zou, Rational and scalable fabrication of high-quality WO3/CdS core/shell nanowire arrays for photoanodes toward enhanced charge separation and transport under visible light, Nanoscale 5 (2013) 11933–11939, https://doi.org/10.1039/c3nr03493c

[5] A. Kuzmin, J. Purans, Local atomic and electronic structure of tungsten ions in AWO4 crystals of scheelite and wolframite types, Radiat. Meas. 33 (2001) 583–586, https://doi.org/10.1016/S1350-4487(01)00063-4

[6] N.F.A. Neto, P.M. Oliveira, M.R.D. Bomio, F.V. Motta, Effect of temperature on the morphology and optical properties of Ag2WO4 obtained by the co-precipitation method: photocatalytic activity, Ceram. Int. 45 (2019) 15205–15212, https://doi.org/10.1016/j.ceramint.2019.05.006

[7] H.P. Marques, A.R. Canário, A.M.C. Moutinho, O.M.N.D. Teodoro, Shaping Ag clusters on Titania, J. Phys. Conf. Ser. 61 (2007) 775–779, https://doi.org/10.1088/1742-6596/61/1/155

[8] B. Liu, Z. Hu, Y. Chen, K. Sun, X. Pan, Y. Che, Ultrafast pulsed laser ablation for synthesis of nanocrystals, nanoengineering: fabrication, properties, Opt., Devices IV 6645 (2007) 66450R, https://doi.org/10.1117/12.736522

[9] K.J. Rao, B. Vaidhyanathan, M. Ganguli, P.A. Ramakrishnan, Synthesis of inorganic solids using microwaves, Chem. Mater. 11 (1999) 882–895, https://doi.org/10.1021/cm9803859

[10] M.A. San-Miguel, E.Z. Da Silva, S.M. Zanetti, M. Cilense, M.T. Fabbro, L. Gracia, J. Andrés, E. Longo, In situ growth of Ag nanoparticles on α-Ag2 WO4 under electron irradiation: probing the physical principles, Nanotechnology 27 (2016), https://doi.org/10.1088/0957-4484/27/22/225703

[11] J.C. Sczancoski, S.M. Johnson, S. Pereira, E. Longo, E.R. Leite, Atomic diffusion induced by electron-beam irradiation: an in situ study of Ag structures grown from α - Ag2 WO4, Cryst. Growth Des. (2018), https://doi.org/10.1021/acs.cgd.8b01076

[12] Y.J. Zhu, F. Chen, Microwave-assisted preparation of inorganic nanostructures in liquid phase, Chem. Rev. 114 (2014) 6462–6555, https://doi.org/10.1021/cr400366s

[13] A. Mirzaei, G. Neri, Microwave-assisted synthesis of metal oxide nanostructures for gas sensing application: a review, Sens. Actuators B Chem. 237 (2016) 749–775, https://doi.org/10.1016/j.snb.2016.06.114

[14] S.C. Motshekga, S.K. Pillai, S. Sinha Ray, K. Jalama, R.W.M. Krause, Recent trends in the microwave-assisted synthesis of metal oxide nanoparticles supported on carbon nanotubes and their applications, J. Nanomater. (2012)) (2012), https://doi.org/10.1155/2012/691503

[15] D. Zhang, Y. Zhang, Y. Fan, N. Luo, Z. Cheng, J. Xu, Micro-spherical ZnSnO3 material prepared by microwave-assisted method and its ethanol sensing properties, Chin. Chem. Lett. 31 (2020) 2087–2090, https://doi.org/10.1016/j.cclet.2020.01.004

[16] R.E. Newnham , S.J. Jang , M. Xu , F. Jones , This Paper Is a Component Part of the Following Compilation Report: Authored Sections of Proceeding, Annals, Symposia, Etc. However, the Component Should Be Considered Within The Context of the Overall Compilation Report and Fundamental Interaction, Ceramic Transactions. Volume 21 Proceedsing Symp. . Microw. Theory Appl. Mater. Process. Annu. Meet. Am. Cermic Soc. (23rd) 21 1991.

[17] T. Sin Tee, T. Chun Hui, C. Wu Yi, Y. Chi Chin, A.A. Umar, G. Riski Titian, L. Hock Beng, L. Kok Sing, M. Yahaya, M.M. Salleh, Microwave-assisted hydrolysis preparation of highly crystalline ZnO nanorod array for room temperature photoluminescence-based CO gas sensor, Sens. Actuators, B Chem. 227 (2016) 304–312, https://doi.org/10.1016/j.snb.2015.12.058

[18] H.W. Kim, Y.J. Kwon, A. Mirzaei, S.Y. Kang, M.S. Choi, J.H. Bang, S.S. Kim, Synthesis of zinc oxide semiconductors-graphene nanocomposites by microwave irradiation for application to gas sensors, Sens. Actuators, B Chem. 249 (2017) 590–601, https://doi.org/10.1016/j.snb.2017.03.149

[19] L. Cruz, M.M. Teixeira, V. Teodoro, N. Jacomaci, L.O. Laier, M. Assis, N.G. Macedo, A.C.M. Tello, L.F. da Silva, G.E. Marques, M.A. Zaghete, M.D. Teodoro, E. Longo, Multi-dimensional architecture of Ag/α-Ag2WO4 crystals: insights into microstructural, morphological, and photoluminescence properties, CrystEngComm 22 (2020) 7903–7917, https://doi.org/10.1039/d0ce00876a

[20] L.O. Laier, M. Assis, C.C. Foggi, A.F. Gouveia, C.E. Vergani, L.C.L. Santana, L.S. Cavalcante, J. Andrés, E. Longo, Surface-dependent properties of α-Ag2WO4: a joint experimental and theoretical investigation, Theor. Chem. Acc. 139 (2020) 1–11, https://doi.org/10.1007/s00214-020-02613-z

[21] N.G. Macedo, A.F. Gouveia, R.A. Roca, M. Assis, L. Gracia, J. Andrés, E.R. Leite, E. Longo, Surfactant-mediated morphology and photocatalytic activity of α-Ag2WO4material, J. Phys. Chem. C 122 (2018) 8667–8679, https://doi.org/10.1021/acs.jpcc.8b01898

[22] M. Assis, R.A. Pontes Ribeiro, M.H. Carvalho, M.M. Teixeira, Y.G. Gobato, G.A. Prando, C.R. Mendonça, L. De Boni, A.J. Aparecido De Oliveira, J. Bettini, J. Andrés, E. Longo, Unconventional magnetization generated from electron beam and femtosecond irradiation on α-Ag2WO4: a quantum chemical investigation, ACS Omega 5 (2020) 10052–10067, https://doi.org/10.1021/acsomega.0c00542

[23] E. Longo, W. Avansi, J. Bettini, J. Andrés, L. Gracia, In situ transmission electron microscopy observation of Ag nanocrystal evolution by surfactant free electron-driven synthesis, Sci. Rep. 6 (2016) 1–8, https://doi.org/10.1038/srep21498

[24] E. Longo, L.S. Cavalcante, D.P. Volanti, A.F. Gouveia, V.M. Longo, J.A. Varela, M.O. Orlandi, J. Andrés, Direct in situ observation of the electron-driven

synthesis of Ag filaments on α-Ag2WO4crystals, Sci. Rep. 3 (2013) 4–7, https://doi.org/10.1038/srep01676
[25] J. Andrés, L. Gracia, P. Gonzalez-Navarrete, V.M. Longo, W. Avansi, D.P. Volanti, M.M. Ferrer, P.S. Lemos, F.A. La Porta, A.C. Hernandes, E. Longo, Structural and electronic analysis of the atomic scale nucleation of Ag on α-Ag2WO4 induced by electron irradiation, Sci. Rep. 4 (2014) 1–7, https://doi.org/10.1038/srep05391
[26] W. da, S. Pereira, J. Andrés, L. Gracia, M.A. San-Miguel, E.Z. da Silva, E. Longo, V.M. Longo, Elucidating the real-time Ag nanoparticle growth on α-Ag2 WO4 during electron beam irradiation: experimental evidence and theoretical insights, Phys. Chem. Chem. Phys. 17 (2015) 5352–5359, https://doi.org/10.1039/c4cp05849f
[27] J. Andrés, A.F. Gouveia, L. Gracia, E. Longo, G. Manzeppi Faccin, E.Z. da Silva, D.H. Pereira, M.A. San-Miguel, Formation of Ag nanoparticles under electron beam irradiation: Atomistic origins from first-principles calculations, Int. J. Quantum Chem. 118 (2018) 1–15, https://doi.org/10.1002/qua.25551
[28] M. Longo, C.C. De Foggi, M.M. Ferrer, A.F. Gouveia, R.S. Andre, W. Avansi, C.E. Vergani, A.L. Machado, J. Andre, A.C. Hernandes, E. Longo, P.O. Box, Potentiated Electron Transference in α - Ag2WO4 microcrystals with Ag nanofi laments as microbial agent, J. Phys. Chem. A (2014), https://doi.org/10.1021/jp410564p
[29] M. Assis, E. Cordoncillo, R. Torres-mendieta, H. Beltrán-mir, G. Mínguez-vega, R. Oliveira, E.R. Leite, C.C. Foggi, C.E. Vergani, E. Longo, J. Andrés, Towards Scale-Form. Nanopart. α -Ag2WO4 bactericidal Prop. femtosecond Laser Irradiat. (2018) 1–11, https://doi.org/10.1038/s41598-018-19270-9
[30] N.G. Macedo, T.R. Machado, R.A. Roca, M. Assis, C.C. Foggi, V. Puerto-Belda, G. Mínguez-Vega, A. Rodrigues, M.A. San-Miguel, E. Cordoncillo, H. Beltrán-Mir, J. Andrés, E. Longo, Tailoring the bactericidal activity of Ag nanoparticles/α-Ag2WO4 composite induced by electron beam and femtosecond laser irradiation: integration of experiment and computational modeling, ACS Appl. Bio Mater. 2 (2019) 824–837, https://doi.org/10.1021/acsabm.8b00673
[31] M. Assis, T. Robeldo, C.C. Foggi, A.M. Kubo, G. Mínguez-Vega, E. Condoncillo, H. Beltran-Mir, R. Torres-Mendieta, J. Andrés, M. Oliva, C.E. Vergani, P.A. Barbugli, E.R. Camargo, R.C. Borra, E. Longo, Ag nanoparticles/α-Ag2WO4 composite formed by electron beam and femtosecond irradiation as potent antifungal and antitumor agents, Sci. Rep. 9 (2019) 1–15, https://doi.org/10.1038/s41598-019-46159-y
[32] E. Longo, D.P. Volanti, V.M. Longo, L. Gracia, I.C. Nogueira, M.A.P. Almdeira, A.N. Pinheiro, M.M. Ferrer, L.S. Cavalcante, J. Andrés, Toward an understanding of the growth of Ag filaments on α-Ag2WO4 and their photoluminescent properties: acombined experimental and theoretical study, J. Phys. Chem. C. 118 (2014) 1229–1239, https://doi.org/10.1021/jp408167v
[33] A. Sreedevi, K.P. Priyanka, K.K. Babitha, S. Ganesh, T. Varghese, Influence of electron beam irradiation on structural and optical properties of α-Ag2WO4 nanoparticles, Micron 88 (2016) 1–6, https://doi.org/10.1016/j.micron.2016.05.003
[34] C.C. dos Santos, M. de Assis, T.R. Machado, P.F. dos Santos Pereira, G. Minguez-Vega, E. Cordoncillo, H. Beltran-Mir, C. Doñate-Buendía, J. Andrés, E. Longo, Proof-of-concept studies directed toward the formation of metallic Ag nanostructures from Ag3PO4 induced by electron beam and femtosecond laser, Part. Part. Syst. Charact. 36 (2019) 1–9, https://doi.org/10.1002/ppsc.201800533
[35] P.S. Lemos, G.S. Silva, R.A. Roca, M. Assis, R. Torres-Mendieta, H. Beltrán-Mir, G. Mínguez-Vega, E. Cordoncillo, J. Andrés, E. Longo, Laser and electron beam-induced formation of Ag/Cr structures on Ag2CrO4, Phys. Chem. Chem. Phys. 21 (2019) 6101–6111, https://doi.org/10.1039/c8cp07263a
[36] C.H.B. Ng, W.Y. Fan, Preparation of highly uniform 1-dimensional α-Ag2WO4 nanostructures with controllable aspect ratio and study of the growth mechanism, CrystEngComm 18 (2016) 8010–8019, https://doi.org/10.1039/c6ce01298a
[37] Z. Lin, J. Li, Z. Zheng, J. Yan, P. Liu, C. Wang, G. Yang, Electronic reconstruction of α-Ag2WO4 nanorods for visible-light photocatalysis, ACS Nano 9 (2015) 7256–7265, https://doi.org/10.1021/acsnano.5b02077
[38] P.F.S. Pereira, A.F. Gouveia, M. Assis, R.C. De Oliveira, I.M. Pinatti, M. Penha, R.F. Gonçalves, L. Gracia, J. Andrés, E. Longo, ZnWO4 nanocrystals: synthesis, morphology, photoluminescence and photocatalytic properties, Phys. Chem. Chem. Phys. 20 (2018) 1923–1937, https://doi.org/10.1039/c7cp07354b
[39] I.M. Pinatti, I.C. Nogueira, W.S. Pereira, P.F.S. Pereira, R.F. Gonçalves, J.A. Varela, E. Longo, I.L.V. Rosa, Structural and photoluminescence properties of Eu3+ doped α-Ag2WO4 synthesized by the green coprecipitation methodology, Dalton Trans. 44 (2015) 17673–17685, https://doi.org/10.1039/c5dt01997d
[40] C.C. de Foggi, R.C. de Oliveira, M.T. Fabbro, C.E. Vergani, J. Andres, E. Longo, A.L. Machado, Tuning the morphological, optical, and antimicrobial properties of α-ag2wo4 microcrystals using different solvents, Cryst. Growth Des. 17 (2017) 6239–6246, https://doi.org/10.1021/acs.cgd.7b00786
[41] A.C.M. Tello, M. Assis, R. Menasce, A.F. Gouveia, V. Teodoro, N. Jacomaci, M.A. Zaghete, J. Andrés, G.E. Marques, M.D. Teodoro, A.B.F. Da Silva, E. Longo, Microwave-driven hexagonal-to-monoclinic transition in BiPO4: an in-depth experimental investigation and first-principles study, Inorg. Chem. 59 (2020) 7453–7468, https://doi.org/10.1021/acs.inorgchem.0c00181
[42] R. Dovesi, A. Erba, R. Orlando, C.M. Zicovich-Wilson, B. Civalleri, L. Maschio, M. Rérat, S. Casassa, J. Baima, S. Salustro, B. Kirtman, Quantum-mechanical condensed matter simulations with CRYSTAL, Wiley Interdiscip. Rev. Comput. Mol. Sci. 8 (2018) 1–36, https://doi.org/10.1002/wcms.1360
[43] A.D. Becke, A new mixing of Hartree–Fock and local density-functional theories, J. Chem. Phys. 98 (2) (1993) 1372–1377, https://doi.org/10.1063/1.464304
[44] E. Aprà, E. Stefanovich, R. Dovesi, C. Roetti, An ab initio Hartree-Fock study of silver chloride, Chem. Phys. Lett. 186 (1991) 329–335, https://doi.org/10.1016/0009-2614(91)90187-E
[45] F. Corà, A. Patel, N.M. Harrison, R. Dovesi, C.R.A. Callow, An ab initio Hartree-Fock study of the cubic and tetragonal phases of bulk tungsten trioxide, J. Am. Chem. Soc. 118 (1996) 12174–12182, https://doi.org/10.1021/ja961514u
[46] L. Valenzano, F.J. Torres, K. Doll, F. Pascale, C.M. Zicovich-Wilson, R. Dovesi, Ab initio study of the vibrational spectrum and related properties of crystalline compounds; the case of CaCO3 calcite, Z. Fur Phys. Chem. 220 (2006) 893–912, https://doi.org/10.1524/zpch.2006.220.7.893
[47] K. Momma, F. Izumi, VESTA: A three-dimensional visualization system for electronic and structural analysis, J. Appl. Crystallogr. 41 (2008) 653–658, https://doi.org/10.1107/S0021889808012016
[48] R.A. Roca, J.C. Sczancoski, I.C. Nogueira, M.T. Fabbro, H.C. Alves, L. Gracia, L.P.S. Santos, C.P. de Sousa, J. Andrés, G.E. Luz, E. Longo, L.S. Cavalcante, Facet-dependent photocatalytic and antibacterial properties of α-Ag2WO4 crystals: combining experimental data and theoretical insights, Catal. Sci. Technol. 5 (2015) 4091–4107, https://doi.org/10.1039/C5CY00331H
[49] R.F. Egerton, P. Li, M. Malac, Radiation damage in the TEM and SEM, Micron 35 (2004) 399–409, https://doi.org/10.1016/j.micron.2004.02.003
[50] M. Assis, N.G. Macedo, T.R. Machado, M.M. Ferrer, A.F. Gouveia, E. Cordoncillo, R. Torres-Mendieta, H. Beltrán-Mir, G. Mínguez-Vega, E.R. Leite, J.R. Sambrano, J. Andrés, E. Longo, Laser/electron irradiation on indium phosphide (InP) semiconductor: promising pathways to in situ formation of indium nanoparticles, Part. Part. Syst. Charact. 35 (2018) 1–10, https://doi.org/10.1002/ppsc.201800237
[51] R.O. Torres-Mendieta, M.M. Teixeira, G. Mínguez-Vega, D. De Souza, Y.G. Gobato, M. Assis, H. Beltrán-Mir, E. Cordoncillo, J. Andrés, M. Černík, E. Longo, Toward expanding the optical response of Ag2CrO4 and Bi2O3 by their laser-mediated heterojunction, J. Phys. Chem. C. 124 (2020) 26404–26414, https://doi.org/10.1021/acs.jpcc.0c08301
[52] V.N. Rai, S.N. Thakur, Physics and Dynamics of Plasma in Laser-Induced Breakdown Spectroscopy, second ed., Elsevier B.V.,, 2020, https://doi.org/10.1016/b978-0-12-818829-3.00004-6
[53] P.M. Skarstad, S. Geller, W4016)8- polyion in the high temperature modification of silver tungstate, Mat. Res. Bull. 10 (8) (1975) 791–799, https://doi.org/10.1016/0025-5408(75)90193-2
[54] L. Yang, J. Wang, Y. Wan, Y. Li, H. Xie, H. Cheng, H.J. Seo, Structure and effective visible-light-driven photocatalytic activity of α-NiMoO4 for degradation of methylene blue dye, J. Alloy. Compd. 664 (2016) 756–763, https://doi.org/10.1016/j.jallcom.2015.10.037
[55] W. Zhu, X. Feng, Z. Wu, Z. Man, On the annealing mechanism in PbWO4 crystals, Phys. B Condens. Matter 324 (2002) 53–58, https://doi.org/10.1016/S0921-4526(02)01269-3
[56] O. Dulub, U. Diebold, G. Kresse, Novel stabilization mechanism on polar surfaces: ZnO(0001)-Zn, Phys. Rev. Lett. 90 (2003) 4, https://doi.org/10.1103/PhysRevLett.90.016102
[57] A. Barbier, G. Renaud, A. Stierle, The NiO (111)-(1×1) surface, Surf. Sci. 402–404 (1998) 757–760, https://doi.org/10.1016/S0039-6028(97)01020-0
[58] C. Ren, R. Yang, Y. Li, H. Wang, Modulating of facets-dependent oxygen vacancies on ceria and its catalytic oxidation performance, Res. Chem. Intermed. 45 (2019) 3019–3032, https://doi.org/10.1007/s11164-019-03776-6
[59] H. He, S. Xue, Z. Wu, C. Yu, K. Yang, G. Peng, W. Zhou, D. Li, Sonochemical fabrication, characterization and enhanced photocatalytic performance of Ag2S/Ag2WO4 composite microrods, Cuihua Xuebao Chin. J. Catal. 37 (2016) 1841–1850, https://doi.org/10.1016/S1872-2067(16)62515-9
[60] F.Y. Xie, L. Gong, X. Liu, Y.T. Tao, W.H. Zhang, S.H. Chen, H. Meng, J. Chen, XPS studies on surface reduction of tungsten oxide nanowire film by Ar + bombardment, J. Electron Spectrosc. Relat. Phenom. 185 (2012) 112–118, https://doi.org/10.1016/j.elspec.2012.01.004
[61] A. Turkovič, D.L. Fox, J.F. Scott, S. Geller, G.F. Ruse, High temperature Raman spectroscopy of silver tetratungstate, Ag8W4O16, Mater. Res. Bull. 12 (1977) 189–195, https://doi.org/10.1016/0025-5408(77)90163-5
[62] S.K. Gupta, K. Sudarshan, P.S. Ghosh, S. Mukherjee, R.M. Kadam, Doping-induced room temperature stabilization of metastable β-Ag2WO4 and origin of visible emission in α- And β-Ag2WO4: low temperature photoluminescence studies, J. Phys. Chem. C 120 (2016) 7265–7276, https://doi.org/10.1021/acs.jpcc.6b00078
[63] I.M. Pinatti, G.R. Fern, E. Longo, T.G. Ireland, P.F.S. Pereira, I.L.V. Rosa, J. Silver, Luminescence properties of α-Ag2WO4 nanorods co-doped with Li+ and Eu3+ cations and their effects on its structure, J. Lumin. 206 (2018) 442–454, https://doi.org/10.1016/j.jlumin.2018.10.104
[64] A.C. Catto, T. Fiorido, É.L.S. Souza, W. Avansi, J. Andres, K. Aguir, E. Longo, L.S. Cavalcante, L.F. da Silva, Improving the ozone gas-sensing properties of CuWO4 nanoparticles, J. Alloy. Compd. 748 (2018) 411–417, https://doi.org/10.1016/j.jallcom.2018.03.104
[65] A.C. Catto, L.F.D. Silva, M.I.B. Bernardi, S. Bernardini, K. Aguir, E. Longo, V.R. Mastelaro, Local structure and surface properties of CoxZn1-xO Thin films for ozone gas sensing, ACS Appl. Mater. Interfaces 8 (2016) 26066–26072, https://doi.org/10.1021/acsami.6b08589
[66] L.S. Cavalcante, M.A.P. Almeida, W. Avansi, R.L. Tranquilin, E. Longo, N.C. Batista, V.R. Mastelaro, M.S. Li, Cluster coordination and photoluminescence properties of α-Ag2WO4 microcrystals, Inorg. Chem. 51 (2012) 10675–10687, https://doi.org/10.1021/ic300948n
[67] M.M. Teixeira, Y.G. Gobato, L. Gracia, L.F. da Silva, W. Avansi, M. Assis, R.C. de Oliveira, G.A. Prando, J. Andrés, E. Longo, Towards a white-emitting phosphor Ca10V6O25 based material, J. Lumin. 220 (2020) 116990, https://doi.org/10.1016/j.jlumin.2019.116990

[68] L.F. Da Silva, A.C. Catto, W. Avansi, A. Mesquita, L.J.Q. Maia, O.F. Lopes, M.S. Li, M.L. Moreira, E. Longo, J. Andrés, V.R. Mastelaro, Unveiling the efficiency of microwave-assisted hydrothermal treatment for the preparation of SrTiO3 mesocrystals, Phys. Chem. Chem. Phys. 21 (2019) 22031–22038, https://doi.org/10.1039/c9cp02893e
[69] S. Yamazoe, Y. Hitomi, T. Shishido, T. Tanaka, XAFS study of tungsten L1- And L3-edges: structural analysis of WO3 species loaded on TiO2 as a catalyst for photooxidation of NH3, J. Phys. Chem. C. 112 (2008) 6869–6879, https://doi.org/10.1021/jp711250f
[70] G. Poirier, F.C. Cassanjes, Y. Messaddeq, S.J.L. Ribeiro, A. Michalowicz, M. Poulain, Local order around tungsten atoms in tungstate fluorophosphate glasses by X-ray absorption spectroscopy, J. Non-Cryst. Solids 351 (2005) 3644–3648, https://doi.org/10.1016/j.jnoncrysol.2005.08.038
[71] D. Wood, J. Tauc, Weak absorption tails in amorphous semiconductors, Phys. Rev. B 5 (8) (1972) 3144–3151, https://doi.org/10.1103/physrevb.5.3144
[72] B. Philips-Invernizzi, Bibliographical review for reflectance of diffusing media, Opt. Eng. 40 (2001) 1082, https://doi.org/10.1117/1.1370387
[73] L. Yang, B. Kruse, Revised Kubelka–Munk theory I theory and application, J. Opt. Soc. Am. A 21 (2004) 1933, https://doi.org/10.1364/josaa.21.001933
[74] A. Sreedevi, K.P. Priyanka, K.K. Babitha, N. Aloysius Sabu, T.S. Anu, T. Varghese, Chemical synthesis, structural characterization and optical properties of nano-phase α- Ag2WO4, Indian J. Phys. 89 (2015) 889–897, https://doi.org/10.1007/s12648-015-0664-1
[75] M. Li, T. Takei, Q. Zhu, B. Kim, J. Li, Morphology tailoring of ZnWO4 Crystallites / architectures and photoluminescence of the doped RE 3+ ions (RE = Sm, Eu, Tb, and Dy), Inorg. Chem. 58 (2019) 9432–9442, https://doi.org/10.1021/acs.inorgchem.9b01271
[76] R. Alvarez-Roca, A.F. Gouveia, C.C. De Foggi, P.S. Lemos, L. Gracia, L.F. Da Silva, C.E. Vergani, M. San-Miguel, E. Longo, J. Andrés, Selective synthesis of α-, β-, and γ-Ag2WO4 polymorphs: promising platforms for photocatalytic and antibacterial materials, Inorg. Chem. 60 (2021) 1062–1079, https://doi.org/10.1021/acs.inorgchem.0c03186
[77] A. Sreedevi, K.P. Priyanka, K.K. Babitha, S.I. Sankararaman, V. Thomas, Synthesis and characterization of silver tungstate/iron phthalocyanine nanocomposite for electronic applications, Eur. Phys. J. B 90 (2017) 1–10, https://doi.org/10.1140/epjb/e2017-80149-9